



Temperature and thermodynamic deformation analysis of the rotors on a twin screw multiphase pump with high gas volume fractions^{*}

Tie-yu GAO, Dong-fang YANG, Feng CAO^{†‡}, Jin-cheng JIAO

(School of Energy and Power Engineering, Xi'an Jiaotong University, Xi'an 710049, China)

[†]E-mail: fcao@mail.xjtu.edu.cn

Received Dec. 2, 2010; Revision accepted June 7, 2011; Crosschecked Aug. 18, 2011

Abstract: The pressure increasing process within a twin screw multiphase pump, under the condition of high gas volume fractions (GVFs), induces large temperature and pressure changes that cause the rotors to deform. Rotor deformations heavily influence the backflow of the multiphase fluid through clearances within the twin screw multiphase pump and these deformations may even lead to pump failures. An accurate temperature and pressure distribution on the screw rotors need be obtained before the deformation analysis can be carried out. By means of small temperature and pressure sensors embedded into the groove at the root of the rotors, the temperatures of 12 points on the rotors and the pressure distributions of a twin screw multiphase pump under high GVFs conditions were recorded. Temperature test results were adopted to perform a heat transfer analysis for determining the temperature distribution on the screw rotors. Then deformation analyses, including thermal deformation, force deformation, and total deformation, were conducted according to the pressure and temperature distributions. Deformation analysis for different materials was also conducted under the same boundary conditions. A material was suggested for the manufacturing of rotors in a twin screw multiphase pump under the condition of high gas volume fractions.

Key words: Multiphase pump, Twin screw rotor, Thermal deformation, Finite element analysis

doi:10.1631/jzus.A1000485

Document code: A

CLC number: TH327

1 Introduction

A multiphase production system (MPS) can reduce the cost of exploring and conveying to about 70% that of a conventional facility, due to the fact that an MPS may handle gas-liquid mixtures via a single flow line to the processing facilities (Neumann, 1990; DalPorto and Larson, 1997). The twin screw multiphase pump is a promising method to meet the requirements of the MPS and the reliability onshore and offshore (Cooper *et al.*, 1999; Mezzedimi *et al.*, 1999). Usually, twin screw pumps operating with low gas volume fractions (GVFs) do not face the problem of

changes in temperature as pressures increase. Under the conditions of high GVFs, however, the increasing pressure can enhance significantly the temperatures of the fluid and rotors. Thus, the compression process within the multiphase pump induces large pressure and temperature changes that cause the rotors to deform. There are several clearances between moving and static parts of the pump and the clearances are very small. Rotor deformations have a heavy influence on the backflow of multiphase fluid through clearances and this may lead to pump failures (Cao *et al.*, 2001). A better understanding of the heat transfer and deformation of rotors within the pump is, therefore, necessary.

Nakashima *et al.* (2006) developed a model to study the effect of temperature rise on performance in the twin screw multiphase pump being developed by petrobras. The model was used to simulate the thermal behavior of casing and rotors during the loss of

[‡] Corresponding author

^{*} Project supported by the National High-Tech R&D Program (863) of China (No. 2007AA05Z208), and the Scientific Research Foundation for Returned Scholars (No. 50706034), China

© Zhejiang University and Springer-Verlag Berlin Heidelberg 2011

prime events faced by the prototype. Kovacevic *et al.* (2002) and Stosic *et al.* (2005) presented a 3D numerical method to calculate flow and deformation of a twin screw compressor simultaneously, which provided essential reference points for investigation of rotor deformation for a twin screw multiphase pump.

The pumping process of multiphase fluids in the twin screw pump is a complex phenomenon where recycling of the multiphase fluid through pump's clearances defines a temperature and pressure profile as well as the performance of pump. Temperature and thermodynamic deformation analyses of the rotor present a challenge when considering a twin screw multiphase pump handling gas-liquid mixtures with high GVF.

led out of the twin screw multiphase pump and then conveniently processed in the dynamic data acquisition system. As a result, a highly accurate pressure distribution can be obtained, as reported by Peng *et al.* (2002). As shown in Fig. 2, a miniature pressure sensor is mounted in the root groove on the discharge side of the female rotor. The pressure fluctuations within the multiphase pump are measured with the sensor in the outlet side to cover as much as possible of the whole process, and the miniature temperature sensors are mounted radial symmetrically in the root grooves of the rotors. There are 12 measuring points as illustrated in Fig. 1. Points A_1 , B_1 , A_2 , and B_2 are selected in the region of rotor immediately prior to the outlet port. On the contrary, points E_1 , F_1 , E_2 , and F_2

2 Method

2.1 Experimental

Fig. 1 presents the measuring system for recording the temperature and pressure. Table 1 shows the geometrical parameters of the investigated twin screw pump. With the aid of a slip ring on the rotational rotor, the pressure and temperature signals are

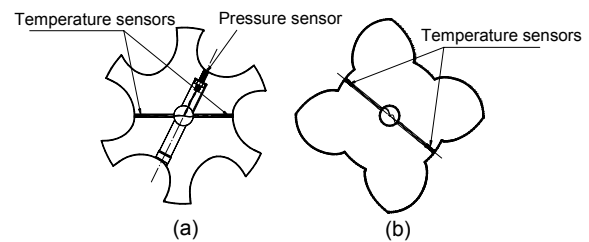


Fig. 2 The position of transducers
(a) Female rotor; (b) Male rotor

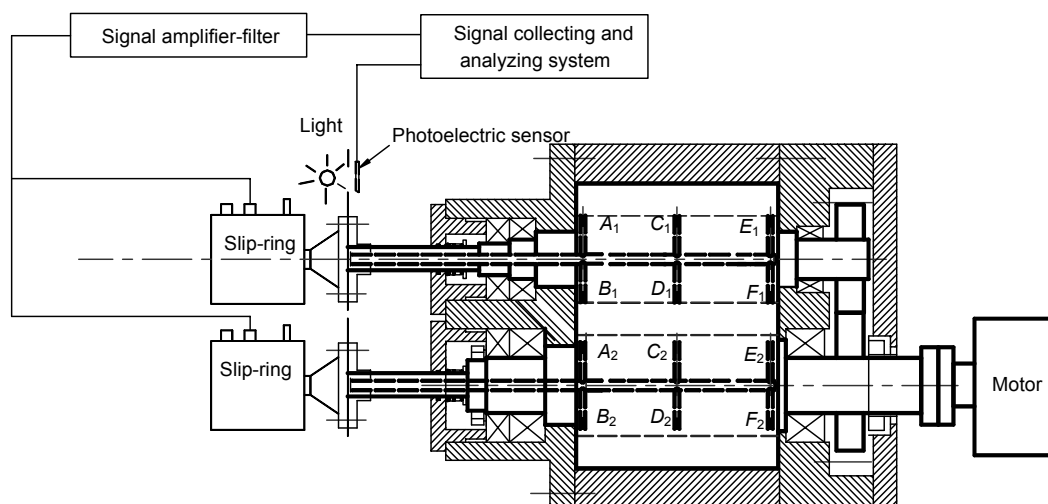


Fig. 1 Transducer installation and data acquisition

Table 1 Main geometric parameters of the multiphase pump

Item	Lobe number	Outer diameter (mm)	Inter diameter (mm)	Wrap angle (°)	Length (mm)
Male rotor	4	105	64	325.0	130
Female rotor	6	96	55	216.7	130

are set in the region of rotor immediately after the inlet port. Points C_1 , D_1 , C_2 , and D_2 are located in the middle section between the outlet and inlet.

Building the sensors into the root grooves makes installation more convenient. The signal wires were connected to the sliding part of the slip ring through a small axially loaded bored hole, as described by Cao *et al.* (2011). The dynamic data acquisition system JOVIAN5200 is used to collect and analyze signal. A photoelectric sensor mounted on the shaft coupling between the slip ring and pump is used to define a phase position of the recorded pressure, and produces an impulse at the beginning of the compression working process (Fig. 1). The pressure distribution versus the rotational angle of the rotor can be obtained with the pressure signal and the position signal. A diagram of pressure distribution versus chamber volume can be achieved using a transformation between the rotational angle of rotor and the volume of working chamber (Xing, 2000). The significance of the effect of the built-in ratio on the performance is shown by plotting the volume abscissa. The basic dimension of the temperature sensor is $\Phi 2.2 \text{ mm} \times 16 \text{ mm}$. The range of the working temperatures of the sensor is from -200 to 550°C , with an overall error of ± 0.15 and 0.2% of the reading. The diameter of the pressure sensor is 4.76 mm . The response frequency of pressure sensor is as high as 500 kHz . The maximum working pressure is 3.5 MPa and the range of working temperature is from -55 to 204°C , with an overall error of $\pm 0.3\%$.

Additionally, two thermocouples are placed at the suction pipe and discharge pipe to measure the temperatures of fluid. Air and mineral oil are used as the fluid, with a ratio of 97:3.

2.2 Results of the temperature measuring experiment

Table 2 shows the measured results obtained for inlet conditions of 0.1 MPa pressure, 25°C temperature and 97% GVF with an outlet pressure of 0.8 MPa . All temperature data recorded around 10 min vary by no more than 0.5°C , demonstrating the temperature distribution of rotors varies within a small range in the steady state. The ultimate values presented are the average of datasets in a period of 10 min . As shown in Table 2, the temperature rise in the multiphase pump is much greater and has an av-

erage value of 116°C at the outlet due to high GVFs of gas-liquid mixtures.

It also can be seen that, due to the high rotational speed and intermittent passing through hot and cold gas fluid areas, the temperatures of rotors are far lower than that of the fluid.

Comparing the temperatures of points A_1 , B_1 , A_2 , and B_2 , it can be seen that the differences of the temperatures are very small. As presented in Table 2, the temperature of point C_1 has almost the same value as points D_1 , C_2 , and D_2 . The temperatures of points E_1 , F_1 , E_2 , and F_2 are nearly identical. This can be explained by the high rotational speed and the high thermal conductivity of the rotors. Therefore, the states of two rotors at the same section seem to be the same.

All the temperatures measured at points A_1 , B_1 , A_2 , B_2 , C_1 , D_1 , C_2 , D_2 , E_1 , F_1 , E_2 , and F_2 in the steady state are used in a finite element analysis to conduct the calculation of the temperature distribution, and the stress and thermal deformations of the screw rotor (Lin *et al.*, 2005).

Fig. 3 shows the pressure distribution measured by the pressure sensor within a full working process. The results of the pressure distribution provide the pressure conditions for the force deformation analysis.

Table 2 Temperature at nodes measured in the experiment

Item	Measured value
Suction pressure, P_{in} (MPa)	0.1
Discharge pressure, P_{out} (MPa)	0.8
Suction temperature, T_{in} ($^\circ\text{C}$)	25
Gas volume fractions	97%
Temperature of point A_1 ($^\circ\text{C}$)	83.0
Temperature of point B_1 ($^\circ\text{C}$)	82.7
Temperature of point C_1 ($^\circ\text{C}$)	79.2
Temperature of point D_1 ($^\circ\text{C}$)	78.9
Temperature of point E_1 ($^\circ\text{C}$)	77.0
Temperature of point F_1 ($^\circ\text{C}$)	76.8
Temperature of point A_2 ($^\circ\text{C}$)	82.6
Temperature of point B_2 ($^\circ\text{C}$)	82.9
Temperature of point C_2 ($^\circ\text{C}$)	79.0
Temperature of point D_2 ($^\circ\text{C}$)	78.7
Temperature of point E_2 ($^\circ\text{C}$)	76.5
Temperature of point F_2 ($^\circ\text{C}$)	76.8
Discharge temperature, T_{out} ($^\circ\text{C}$)	116
Rotational speed, n (r/min)	2400

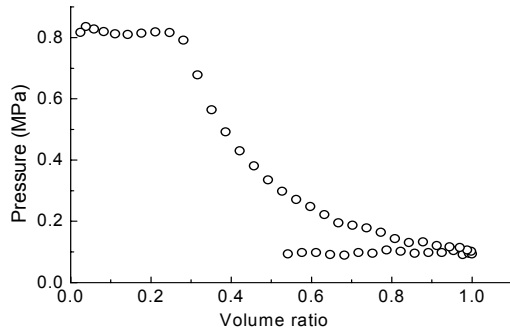


Fig. 3 Pressure diagram vs. built-in ratio
 $n=2400$ r/min, $P_{in}=0.1$ MPa, and GVF=97%

3 Heat transfer analysis

3.1 Material properties

The rotors are made from gray cast iron HT200, whose material properties are listed in Table 3.

Table 3 Properties of gray cast iron HT200

Parameter	Value
Elasticity modulus (GPa)	110
Poisson ratio	0.26
Density (kg/m^3)	7.80×10^3
Coefficient of expansion (K^{-1})	1.30×10^{-5}
Coefficient of heat transfer ($\text{W}/(\text{m} \cdot \text{K})$)	50.3
Specific heat ($\text{kJ}/(\text{kg} \cdot \text{K})$)	0.67
Tensile strength (MPa)	200

3.2 Boundary conditions

The finite element simulation, implemented within an ANSYS environment, was performed by using the experimental rotor temperatures and heat transfer coefficient between the rotor surface and working fluid as a boundary condition.

The experimental rotor temperatures are the corresponsive temperatures of points A_1 , B_1 , A_2 , B_2 , C_1 , D_1 , C_2 , D_2 , E_1 , F_1 , E_2 , and F_2 in the steady state. Because of the high rotational speed of rotors, the temperatures at the nodes within the hollow cylinder, as shown in black color in Fig. 4, can be considered the same as the corresponsive measured temperature. The average temperatures of the points A_1 and B_1 , C_1 and D_1 , E_1 and F_1 , A_2 and B_2 , C_2 and D_2 , and E_2 and F_2 , are used as the first boundary conditions for six hollow cylinders of female and male rotors. The size of the hollow cylinders corresponds to the size of sensors.

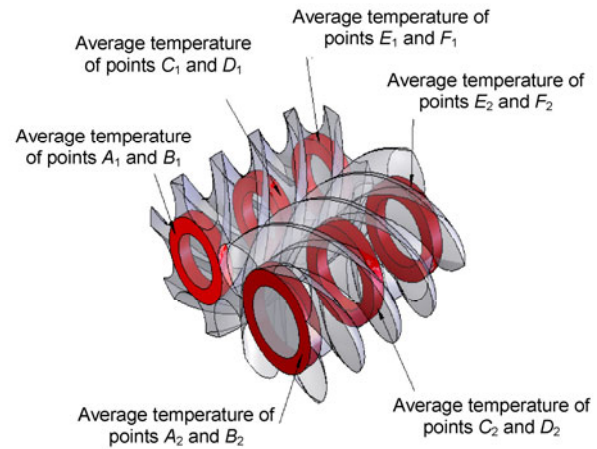


Fig. 4 Sketch of boundary conditions for heat transfer analysis

In the steady state, the heat received from the fluid in the discharge section of the rotor will be dissipated to the fluid in the region of the suction section. The rotor is in thermal equilibrium.

Due to centrifugation, the liquid is concentrated at the rotor periphery. It is assumed that only a single liquid phase exists at the rotor periphery. Except for tips, screw teeth are filled with the two-phase working fluid.

The convection heat transfer coefficient between screw tips and liquid α is calculated using the well-known Dittus-Boelter correlation (Dittus and Boelter, 1930/1985):

$$\alpha = 0.023(\lambda / d)Re^{0.8}Pr^z, \quad (1)$$

where λ is the coefficient of heat conductivity, d is the equivalent diameter. z is a constant, $z=0.3$ for cooling the fluid and $z=0.4$ for heating the fluid.

The forced convection heat transfer coefficient between the screw teeth and gas-liquid mixture α_{tp} can be calculated (Dittus and Boelter, 1930/1985):

$$\alpha_{tp} = (12.76X_{tt}^4 - 27.70X_{tt}^3 + 11.02X_{tt}^2 + 5.29X_{tt} + 0.55)\alpha, \quad (2)$$

$$X_{tt} = \left[\left(\frac{1-x}{x} \right)^{1.8} \frac{\rho_g \mu_l}{\rho_l \mu_g} \right]^{0.5}, \quad (3)$$

where tp represent two phase fluid; X_{tt} is the parameter related to two phase fluid; x is the void

fraction of the fluid; ρ_g and ρ_l represent the densities of gas phase and liquid phase, respectively; μ_g and μ_l represent the dynamic viscosities of gas phase and liquid phase, respectively.

3.3 Results of heat transfer analysis

Two views of the detailed temperature distribution for the rotors are shown in Fig. 5, one from the Z - X plane view of the rotor and the other one from a sectional view of the rotor. As can be seen in the rotor temperature distribution, heat transfer occurs mainly from the outlet to inlet region due to a higher discharge temperature. The temperature of the screw tip is higher than that of the screw tooth in the discharge section, especially at the area near the discharge port. In the suction section, however, this trend is reversed. The heat transfer coefficient tends to be higher in the tips than in the screw roots. Also, the screw teeth are similar to fins that enforce heat transfer. The two

factors cause the temperature differences between the roots and the tips. On the other hand, because of the small temperature difference between the rotor and working fluid in the middle section, almost no difference can be seen between the temperatures of screw tips and screw teeth.

4 Deformation analysis

4.1 Boundary conditions

The following constraints are applied to the deformation analysis according to the construction of the real rotors.

1. The freedoms in X , Y , and Z directions in the surface of shafts on discharge side of both rotors are constrained.
2. The freedoms in X and Y directions in the surface of shafts on suction side of both rotors are constrained.

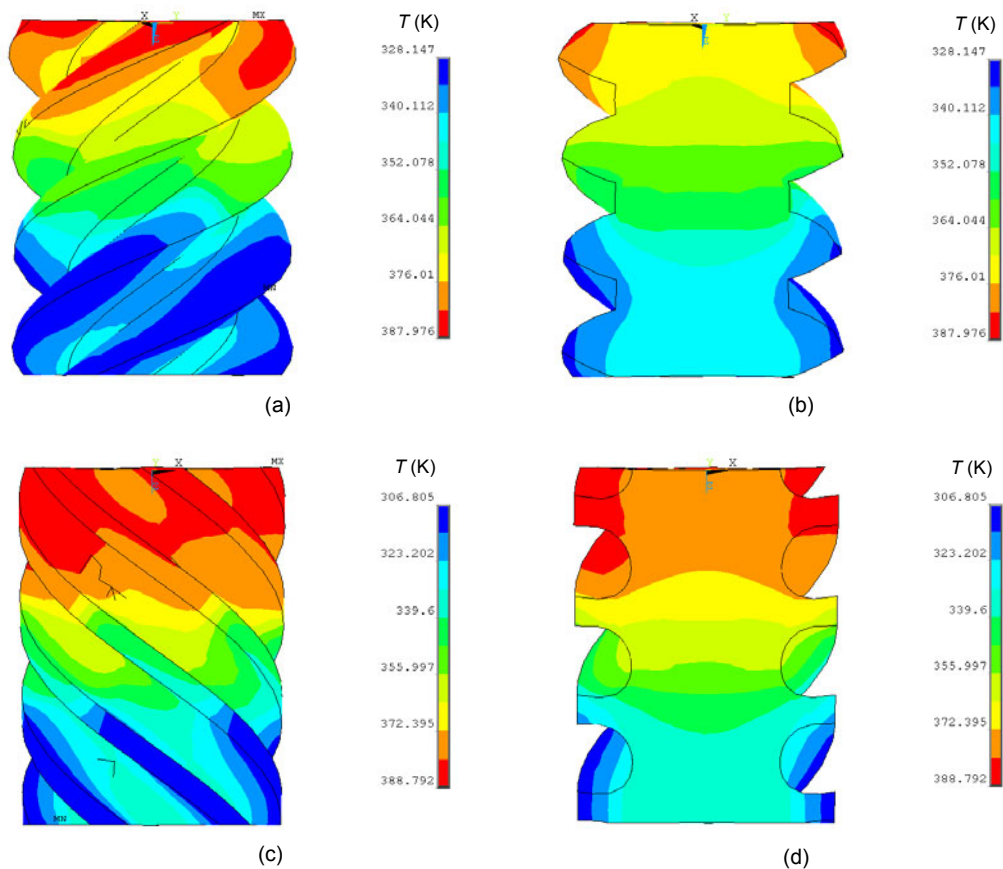


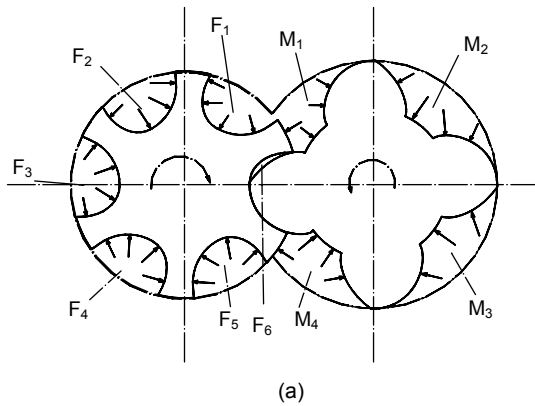
Fig. 5 Steady temperature distributions of rotors

(a) Distribution of male rotor from the Z - X plane view; (b) Distribution of male rotor from the sectional view; (c) Distribution of female rotor from the Z - X plane view; (d) Distribution of male rotor from the sectional view

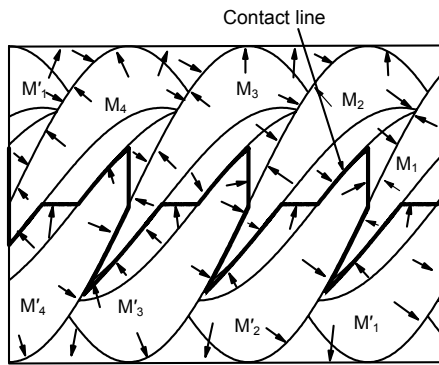
3. The male rotor is driven by the motor, and the female rotor is driven through the synchronous gear. Thus, no contact pressure between the two rotors is assumed in the force deformation analysis.

4. From Fig. 3, the relationship of the pressure inside the chamber and the rotational angle, $p=f(\theta)$, can be obtained. In Fig. 6a, the order of meshing chambers is from F_1 to F_6 for the female rotor and M_1

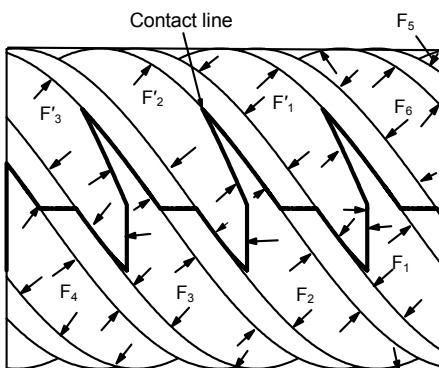
to M_4 for the male rotor. F'_1 to F'_3 represents the meshing chambers for the female rotor on the other side of meshing line corresponding to F_1 to F_3 . M'_1 to M'_4 represent the meshing chamber for the male rotor on the other side of meshing line corresponding to M_1 to M_4 . Assuming the pressures of chambers F_1 and M_1 are expressed by $p_{F_1} = p_{M_1} = f(\theta_m)$, where θ_m is the rotational angle of male rotor. The pressures of different chambers indicated in Fig. 6 are shown in Table 4.



(a)



(b)



(c)

Fig. 6 Sketches of pressure distributions
(a) Outlet section; (b) Male rotor; (c) Female rotor

Table 4 Pressure of different chambers

Male rotor	Female rotor
$p_{M'_1} = f(\theta_m - 180^\circ)$	$p_{F'_1} = f(\theta_m - 180^\circ)$
$p_{M'_2} = f(\theta_m - 90^\circ)$	$p_{F'_2} = f(\theta_m - 60^\circ)$
$p_{M'_3} = f(\theta_m - 270^\circ)$	$p_{F'_3} = f(\theta_m - 240^\circ)$
$p_{M_3} = f(\theta_m - 180^\circ)$	$p_{F_3} = f(\theta_m - 120^\circ)$
$p_{M_3} = f(\theta_m - 360^\circ)$	$p_{F_3} = f(\theta_m - 300^\circ)$
$p_{M_4} = f(\theta_m - 270^\circ)$	$p_{F_4} = f(\theta_m - 180^\circ)$
$p_{M_4} = f(\theta_m - 540^\circ)$	$p_{F_4} = f(\theta_m - 240^\circ)$
	$p_{F_6} = f(\theta_m - 300^\circ)$

4.2 Thermal deformation analysis

Fig. 7 is the detailed thermal deformations of male and female rotors at 0° rotational angle. The deformation value, ε , is obtained by the original coordinates, subtracting from the coordinates after thermal deforming. As shown in Fig. 7, the thermal deformation in X direction is axisymmetric. The thermal deformation in Y direction has the same trend as that in X direction. The region of the maximum deformation in X or Y deformation is located at a point one-fourth of the overall rotor length upstream of the discharge section. The greatest deformation in Z direction is much larger than those in X and Y directions. Thus, for both rotors, the overall thermal deformation has the same trend as that in Z direction.

4.3 Force deformation analysis

Fig. 8 (p.727) shows the force deformation of male and female rotors at 0° rotational angle. It can be seen that the force deformation is not as regular as the thermal deformation. The greatest deformations tend to be larger in Z direction than in X and Y directions. The female rotor is weaker than the male rotor, and therefore deforms more. The overall force deformation results in an enlarging clearance between rotors.

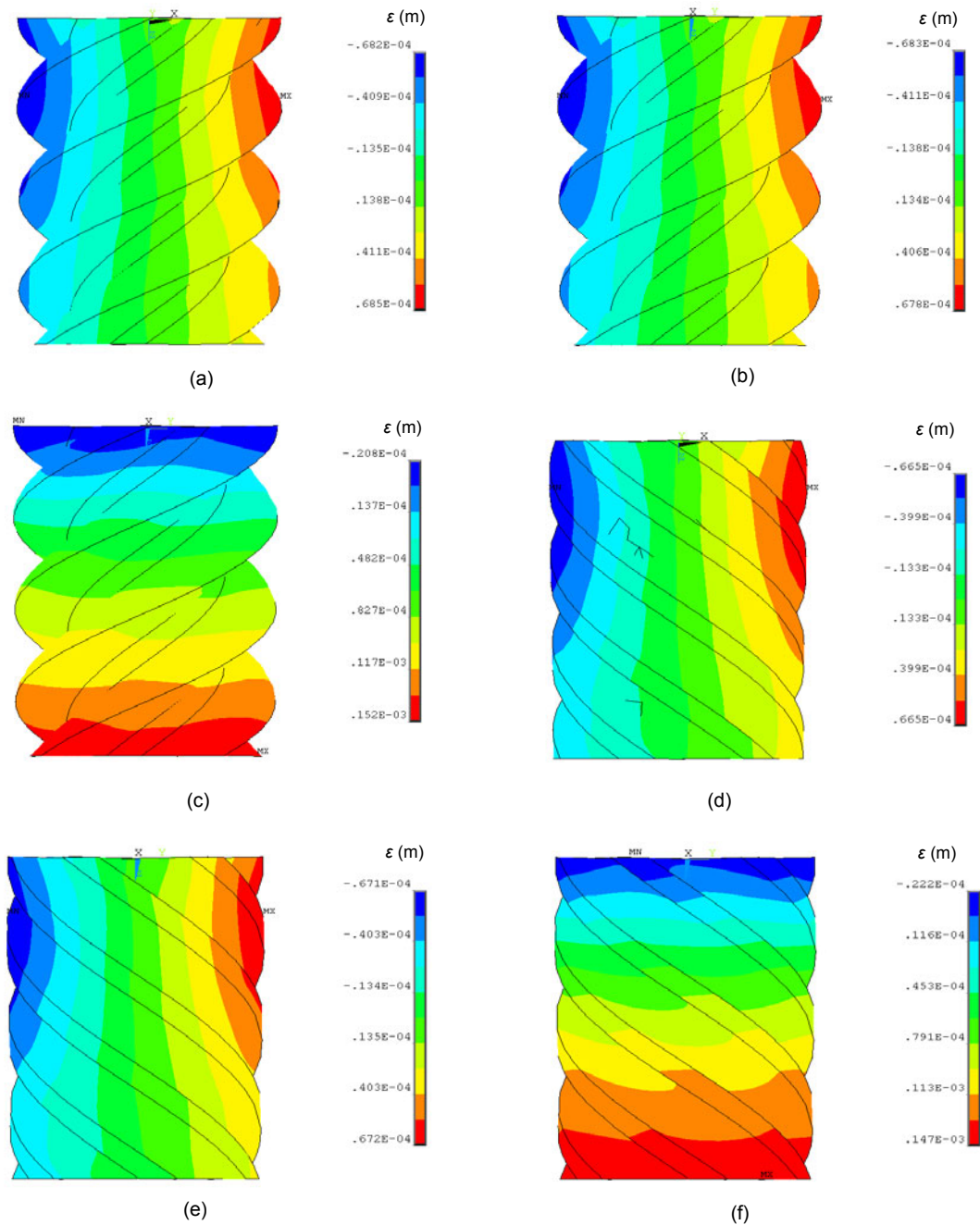


Fig. 7 Thermal deformation distributions of rotors

(a) Deformation of male rotor in X direction; (b) Deformation of male rotor in Y direction; (c) Deformation of male rotor in Z direction; (d) Deformation of female rotor in X direction; (e) Deformation of female rotor in Y direction; (f) Deformation of female rotor in Z direction

4.4 Total deformation analysis

Fig. 9 (p.728) shows the total deformations of the rotors, where the rotational speed, the inlet/outlet pressure, and GVFs are kept constant at 2400 r/min, 0.1 MPa/0.8 MPa, and 97%, respectively.

As shown in Figs. 7–9, the effects of a pressure difference on deformation are negligible compared to the deformation caused by the temperature change, which has the effect of enlarging the rotors, especially in the outlet area. Thus, the total deformation patterns

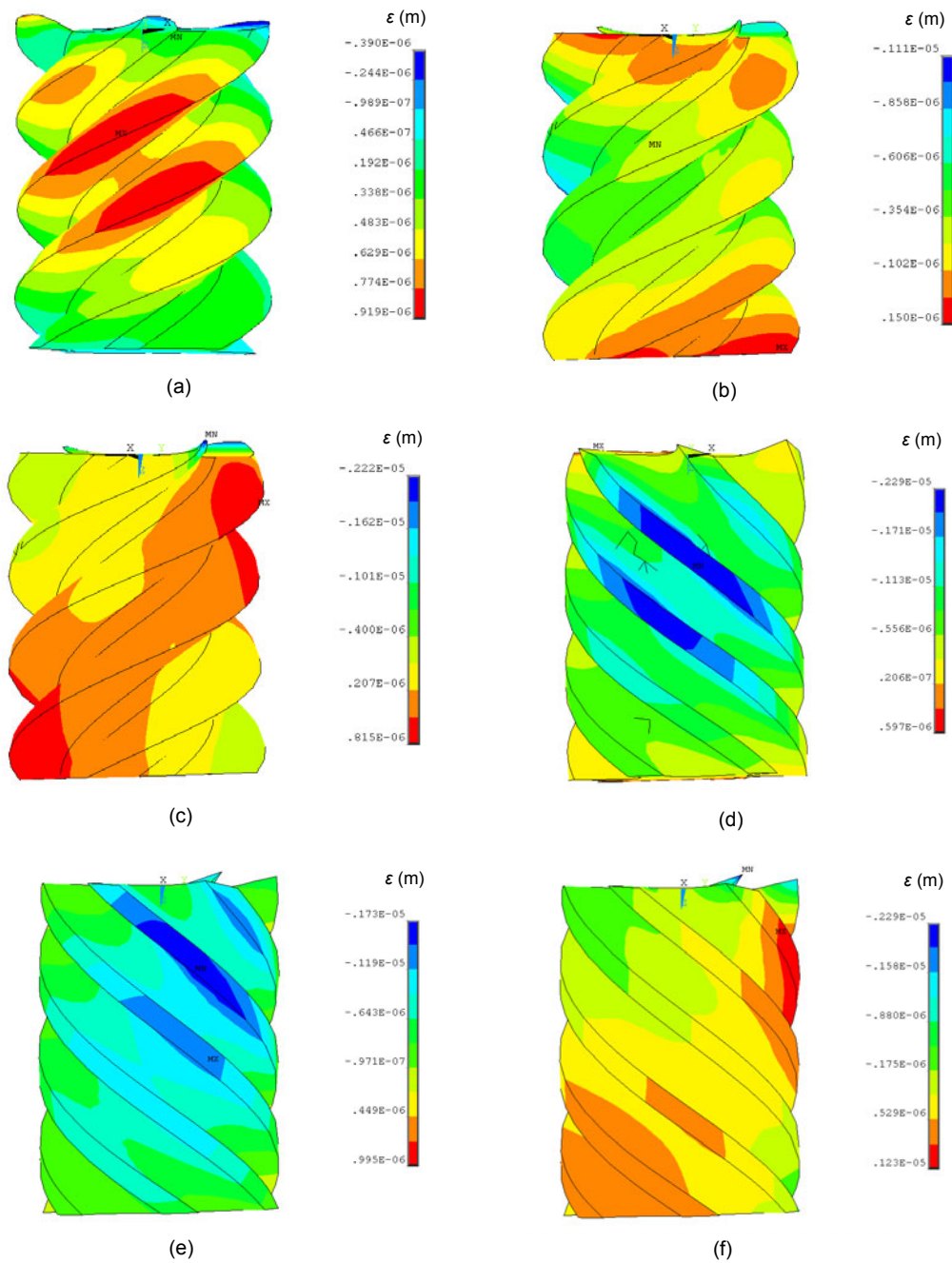


Fig. 8 Force deformation distributions of rotors

(a) Deformation of male rotor in X direction; (b) Deformation of male rotor in Y direction; (c) Deformation of male rotor in Z direction; (d) Deformation of female rotor in X direction; (e) Deformation of female rotor in Y direction; (f) Deformation of female rotor in Z direction

of the rotors are similar to the thermal deformation case, but with a slight enlargement at the direction of the separation of the rotors. Because the freedoms in X , Y , and Z directions in the surface of the shafts on the discharge side of both rotors are constrained, it can be seen that the greatest deformation occurs

in the suction section of rotor. The greatest deformation in Z direction is much larger than those in X and Y directions. The deformation results can be used as reference for rotor and clearance design. Above all, the greatest deformation of rotors in Z direction should be given more attention.

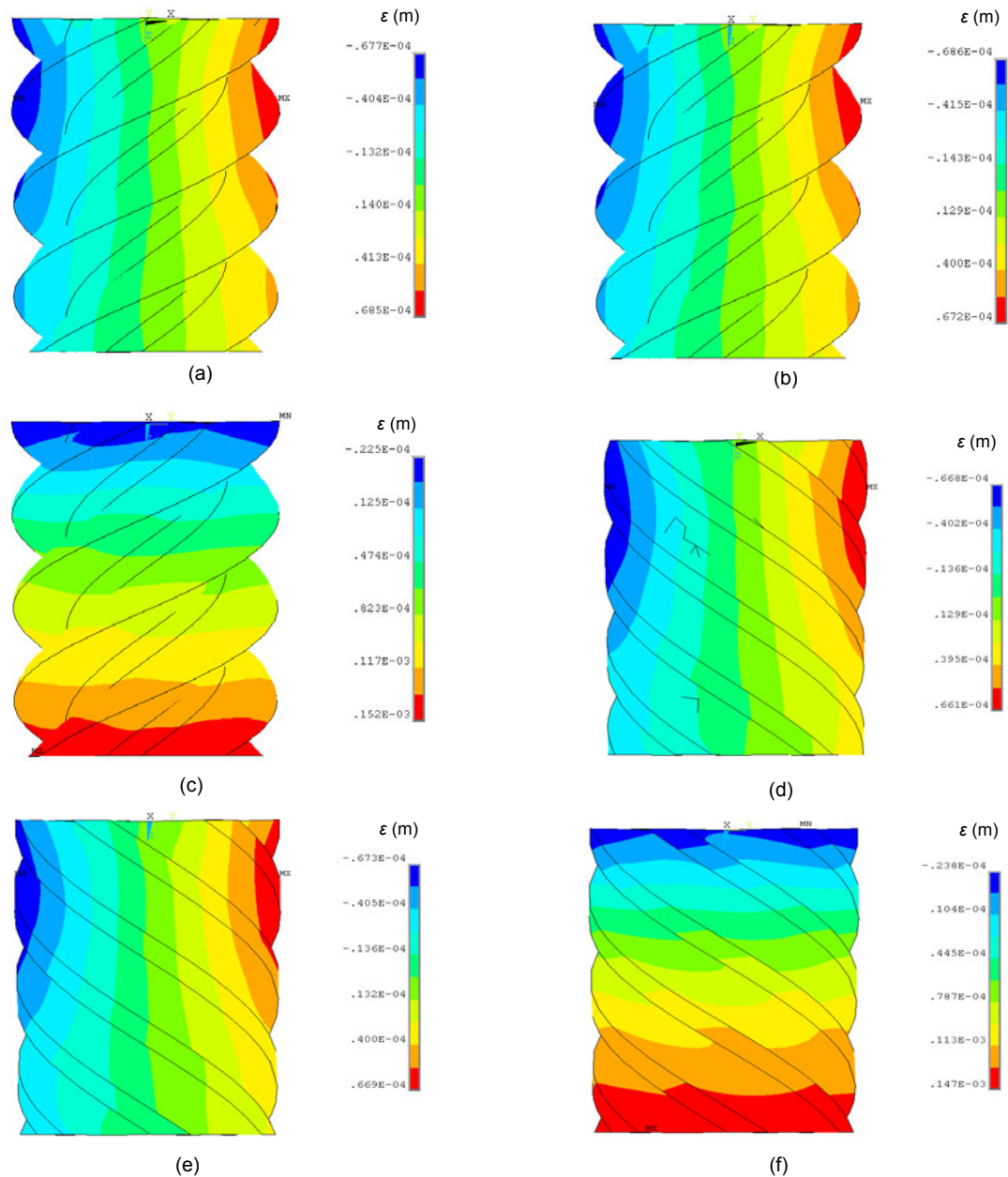


Fig. 9 Total deformation distributions of rotors

(a) Deformation of male rotor in X direction; (b) Deformation of male rotor in Y direction; (c) Deformation of male rotor in Z direction; (d) Deformation of female rotor in X direction; (e) Deformation of female rotor in Y direction; (f) Deformation of female rotor in Z direction

4.5 Deformation analysis for different materials

Deformation analysis for different materials, such as the alloy of steel 38CrMoAl, stainless steel 1Cr18Ni9, carbon steel T10, and the alloy of aluminum 7050, was performed under the same boundary

conditions. The properties for different materials are illustrated in Tables 2 and 5. A comparison of the maximum total deformations for different materials is illustrated in Fig. 10. It can be seen that the rotor made of the alloy of steel, 38CrMoAl, has the least extent of deformation.

Table 5 Properties of different materials*

Type of materials	Specific heat (kJ/(kg·K))	Elasticity modulus (GPa)	Poisson ratio	Coefficient of expansion (K^{-1})	Density (kg/m^3)	Coefficient of heat transfer ($W/(m \cdot K)$)
38CrMoAl	0.50	210	0.30	1.12×10^{-5}	7.90×10^3	60.5
T10	0.46	200	0.29	1.31×10^{-5}	7.87×10^3	51.9
1Cr18Ni9	0.50	193	0.25	1.87×10^{-5}	7.86×10^3	21.5
7050	0.86	71.7	0.33	2.54×10^{-5}	2.83×10^3	155.0

* The properties of HT200 are shown in Table 3

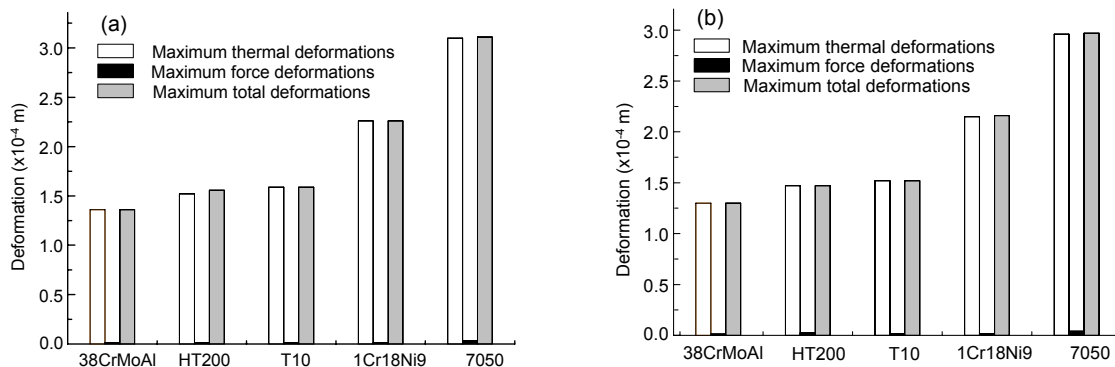


Fig. 10 Deformation analysis for different materials
(a) Deformations of male rotors; (b) Deformations of female rotors

5 Conclusions

In this study, a method was developed to measure the temperatures of 12 points on rotors and the pressure distributions within a twin screw multiphase pump. The temperatures of the 12 points on the rotors and the pressure distributions of a multiphase pump under 97% GVFs conditions were recorded successfully by means of small pressure and temperature sensors embedded into the groove at the root of the rotors. The measures of temperature were adopted to perform a heat transfer analysis for yielding the temperature distribution of the screw rotors. Then deformation analyses, including thermal deformation, force deformation, and total deformation were performed according to the temperature. These procedures can be extended to other screw pumps with different operating conditions and dimensions.

The temperature tends to be higher at the tips than in the screw roots in the discharge and suction sections. In the middle section, however, almost no difference exists between the temperatures of screw tips and screw teeth.

The effects of pressure differences on deformation are negligible compared to the deformation caused

by the temperature change, which has the effect of enlarging the rotors, especially in the outlet area. Thus, the total deformation patterns of the rotors are similar to the thermal deformations case, but with a slight enlargement at the direction of separation of rotors. The greatest deformation of the rotors in Z direction should be given more attention.

Deformation analysis for different materials was performed under the same boundary conditions. The material of 38CrMoAl is suggested for rotor manufacturing of twin screw multiphase pumps under the condition of high GVFs.

References


- Cao, F., Peng, X., Xing, Z., Shu, P., 2001. Thermodynamic performance simulation of a twin-screw multiphase pump. *Proceedings of the Institution of Mechanical Engineers—Part E: Journal of Process Mechanical Engineering*, **215**(E2):157-163.
- Cao, F., Gao, T., Li, S., Xing, Z., Shu, P., 2011. Experimental analysis of pressure distribution in a twin screw compressor for multiphase duties. *Experimental Thermal and Fluid Science*, **35**(1):219-225. [doi:10.1016/j.expthermflusci.2010.09.004]
- Cooper, P., Prang, A.J., Thamsen, P.U., 1999. Applying Multiphase Screw Pumps Subsea. Seventh European Congress on Fluid Machinery for the Oil, Petrochemical,


- and Related Industries, Hague, the Netherlands, p.79-95.
- DalPorto, D.F., Larson, L.A., 1997. Multiphase-pump field trials demonstrate practical applications for the technology. *SPE Production & Facilities*, **12**(3):159-164.
- Dittus, F.W., Boelter, L.M.K., 1930. Heat Transfer in Automobile Radiators of the Tubular Type. *University of California (Berkeley) Publications on Engineering*, **2**(1):443-461; *International Communications in Heat and Mass Transfer* (1985), **12**:3-22.
- Kovacevic, A., Stosic, N., Smith, I.K., 2002. Influence of Rotor Deflection upon the Screw Compressor Process. Conference on Screw Type Machines VDI-Schraubenmaschinen, Dortmund, Germany, p.17-28.
- Lin, C., Chang, Y., Liang, K., Hung, C., 2005. Temperature and thermal deformation analysis on scrolls of scroll compressor. *Applied Thermal Engineering*, **25**(11-12): 1724-1739. [doi:10.1016/j.applthermaleng.2004.11.008]
- Mezzedimi, V., Ranieri, P., Aggradi, G.F., 1999. A Solution for Deepwater Multiphase Boosting. Seventh European Congress on Fluid Machinery for the Oil, Petrochemical and Related Industries, Hague, the Netherlands, p.197-206.
- Nakashima, C.Y., Oliveira, S.Jr., Caetano, E.F., 2006. Heat transfer in a twin-screw multiphase pump: Thermal modeling and one application in the petroleum industry. *Energy*, **31**(15):3415-3425. [doi:10.1016/j.energy.2006.03.007]
- Neumann, W., 1990. Efficient Multiphase Pump Station for Onshore Application and Prospects for Offshore Application. Proceedings of the Eighth International Pump User Symposium, College station, Texas, USA, p.43-48.
- Peng, X., Xing, Z., Cui, T., Li, L., 2002. Analysis of the working process in an oil-flooded screw compressor by means of an indicator diagram. *Proceedings of the Institution of Mechanical Engineers, Part A: Journal of Power and Energy*, **216**(6):465-470. [doi:10.1243/095765002761034230]
- Stosic, N., Smith, I.K., Kovacevic, A., 2005. Numerical Investigation of Heat Transfer on Screw Compressor Rotors. MECOM VII Argentinian Congress on Computational Mechanics, Buenos Aires, Argentina, p.1123-1134.
- Xing, Z., 2000. Screw Compressors: Theory, Design and Application. China Machine Press, Beijing, China, p.71-78 (in Chinese).


2010 JCR of Thomson Reuters for JZUS-A and JZUS-B

ISI Web of KnowledgeSM


Journal Citation Reports[®]

 WELCOME

 HELP


 RETURN TO LIST

2010 JCR Science Edition



Journal: Journal of Zhejiang University-SCIENCE A

Mark	Journal Title	ISSN	Total Cites	Impact Factor	5-Year Impact Factor	Immediacy Index	Citable Items	Cited Half-life	Citing Half-life
<input type="checkbox"/>	J ZHEJIANG UNIV-SC A	1673-565X	442	0.322		0.050	120	3.7	7.1



Journal: Journal of Zhejiang University-SCIENCE B

Mark	Journal Title	ISSN	Total Cites	Impact Factor	5-Year Impact Factor	Immediacy Index	Citable Items	Cited Half-life	Citing Half-life
<input type="checkbox"/>	J ZHEJIANG UNIV-SC B	1673-1581	770	1.027		0.137	124	3.5	7.5